The Cryosphere, 9, 1–11, 2015
www.the-cryosphere.net/9/1/2015/
doi:10.5194/tc-9-1-2015

The Cryosphere
Open Access

UAV photogrammetry and structure from motion to assess calving dynamics at Store Glacier, a large outlet draining the Greenland ice sheet

J. C. Ryan[1], A. L. Hubbard[2], J. E. Box[3], J. Todd[4], P. Christoffersen[4], J. R. Carr[1], T. O. Holt[1], and N. Snooke[5]

[1]Centre for Glaciology, Institute of Geography and Earth Sciences, Aberystwyth University, Aberystwyth, SY23 3DB, UK
[2]Department of Geology, University of Tromsø, 9037 Tromsø, Norway
[3]Geological Survey of Denmark and Greenland, Copenhagen, Denmark
[4]Scott Polar Research Institute, University of Cambridge, Cambridge, UK
[5]Department of Computer Science, Aberystwyth University, Aberystwyth, SY23 3DB, UK

Correspondence to: J. C. Ryan (jor44@aber.ac.uk)

Received: 29 March 2014 – Published in The Cryosphere Discuss.: 28 April 2014
Revised: 25 August 2014 – Accepted: 25 November 2014 – Published: 6 January 2015

Abstract. This study presents the application of a cost-effective, unmanned aerial vehicle (UAV) to investigate calving dynamics at a major marine-terminating outlet glacier draining the western sector of the Greenland ice sheet. The UAV was flown over Store Glacier on three sorties during summer 2013 and acquired over 2000 overlapping, geotagged images of the calving front at an ~ 40 cm ground sampling distance. Stereo-photogrammetry applied to these images enabled the extraction of high-resolution digital elevation models (DEMs) with vertical accuracies of ± 1.9 m which were used to quantify glaciological processes from early July to late August 2013. The central zone of the calving front advanced by ~ 500 m, whilst the lateral margins remained stable. The orientation of crevasses and the surface velocity field derived from feature tracking indicates that lateral drag is the primary resistive force and that ice flow varies across the calving front from 2.5 m d^{-1} at the margins to in excess of 16 m d^{-1} at the centreline. Ice flux through the calving front is 3.8×10^7 m^3 d^{-1}, equivalent to 13.9 Gt a^{-1} and comparable to flux-gate estimates of Store Glacier's annual discharge. Water-filled crevasses were present throughout the observation period but covered a limited area of between 0.025 and 0.24 % of the terminus and did not appear to exert any significant control over fracture or calving. We conclude that the use of repeat UAV surveys coupled with the processing techniques outlined in this paper have great potential for elucidating the complex frontal dynamics that characterise large calving outlet glaciers.

1 Introduction

Observational and modelling studies have demonstrated that Greenland's marine outlet glaciers have a complex and potentially non-linear response to both environmental forcing (e.g. Vieli et al., 2000; Benn et al., 2007; Holland et al., 2008; Howat et al., 2010; Hubbard, 2011; Joughin et al., 2012; Walter et al., 2012; Carr et al., 2013) and to changes in front position (Howat et al., 2007; Luckman et al., 2006; Joughin et al., 2008). To quantify these processes and feedbacks, regular and accurate high-resolution measurements are required to capture the key spatio-temporal linkages between rates of ice calving, flow, surface lowering and frontal advance/retreat. Despite significant advances in satellite remote sensing, limitations of spatial resolution (e.g. MODIS) and/or frequency of repeat imagery (e.g. Landsat or TerraSar-X) render detailed, day-to-day analysis of calving-front dynamics unfeasible. On the other hand, acquisition of digital imagery from unmanned aerial vehicles (UAVs) combined with the development of stereo-photogrammetry software has enabled the provision of high-resolution 3-D georeferenced data on demand for geoscience applications (e.g. d'Oleire-Oltmanns et al., 2012; Hugenholtz et al., 2012, 2013; Whitehead et al., 2013; Lucieer et al., 2014). This represents a cost-effective technique technique for acquiring aerial data in remote, hazardous and/or inaccessible regions and recent applications for emerging snow and ice investigation abound the web (e.g. see the highly informative site of Matt

Table 1. Attributes of the flight surveys and image acquisition of the UAV.

Flight no.	Date	Interval between pictures (s)	No. images	Glacier coverage (km^2)	Resolution of DEM (cm/pixel)
1	1 July	1.55	611	3.17	40
2	2 July	1.51	1051	4.95	38
3	23 August	2.36	567	5.02	39

Nolan; http://www.drmattnolan.org/photography/2013/). To date, published (peer-reviewed) application appears to be limited to the investigation of inter-annual changes of a land-terminating glacier on Bylot Island, Canadian Arctic (Whitehead et al., 2013).

Between July and August 2013, an off-the-shelf, fixed wing UAV equipped with a compact digital camera flew three sorties over the calving front of Store Glacier, West Greenland. The aerial photographs obtained during these flights were used to produce high-resolution (∼ 40 cm; Table 1) digital elevation models (DEMs) and orthophotos of the glacier terminus. These data allowed for the investigation of the spatially complex and time-varying glaciological processes operating at the glacier's calving front. The aim of this paper is to

1. detail the UAV, in terms of its payload and camera settings, and its specific deployment to Store Glacier;
2. describe the techniques used for processing the aerial images and quantifying glaciological processes;
3. discuss the significance of the data we obtained which includes calving events, the character, orientation and morphology of crevasses, surface velocities, ice discharge and changes in thickness and position of the calving front.

2 Data and methods

2.1 Study site

Store Glacier is a large marine-terminating (tidewater) outlet glacier located in the Uummannaq district of West Greenland (Fig. 1). The calving front has a width of 5.3 km and an aerial calving front (freeboard) of up to 110 m a.s.l. (Ahn and Box, 2010). Aerial photography from 1948 onwards reveals that Store Glacier's frontal position has remained stable over the last 65 years (Weidick, 1995). Seasonally, the calving front exhibits advance and retreat of up to 400 m (Howat et al., 2010). The study here focuses specifically on glacier dynamics during the melt season under open-water, tidal modulation of ice flow.

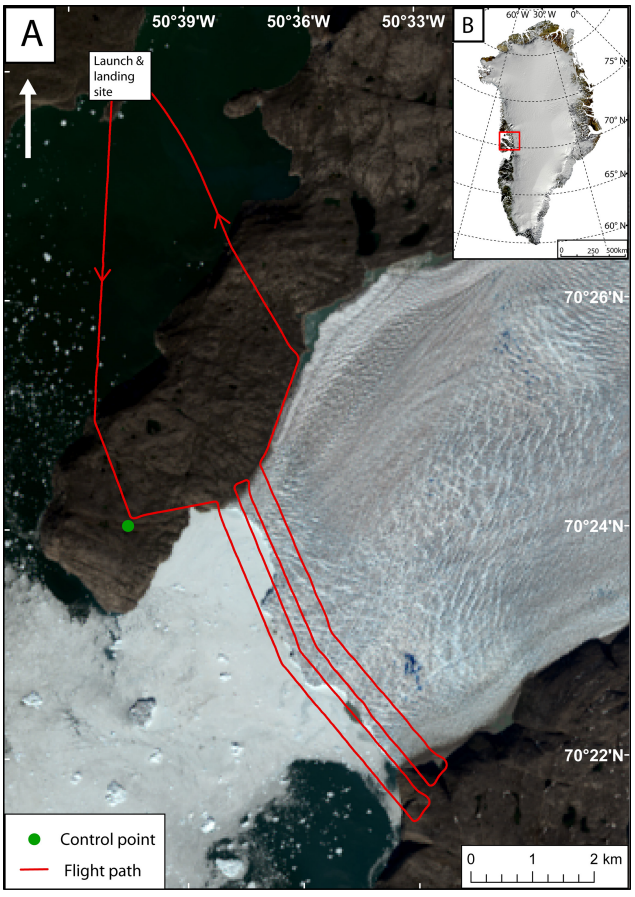

Figure 1. (a) A typical UAV sortie over Store Glacier. The background map is a Landsat 8 true colour image from 12 June 2013. The red line shows the UAV flight path on the 2 July 2013. **(b)** Location of Store Glacier in the Uummannaq region, West Greenland on a MODIS mosaic image of Greenland (Kargel et al., 2012).

2.2 UAV platform

The UAV airframe is an off-the-self Skywalker X8 (www.hobbyking.com) which has a wingspan of 2.12 m and is made from expanded polypropylene (EPP) foam (Fig. 2). For this deployment, the X8 was powered by two 5Ah four-cell (14.8 V) lithium polymer batteries driving a 910 W brushless electric motor turning an 11×7 foldable propeller. In this configuration, the X8 has a flying mass of ∼ 3 kg (including 1 kg payload), which allows for a cruising speed of around 55–70 km per hour with a maximum range of ∼ 60 km in benign conditions at constant altitude. A small propeller/high-revolution motor combination was chosen to provide maximum instantaneous thrust to ensure a clean launch (for novice operators) and to handle the potentially strong katabatic winds encountered during its 40 km sortie.

The autopilot is an open-source project called Ardupilot (http://ardupilot.com/) based on an Atmel 2560 8 bit microcontroller and standard radio control parts including 2.4 GHz

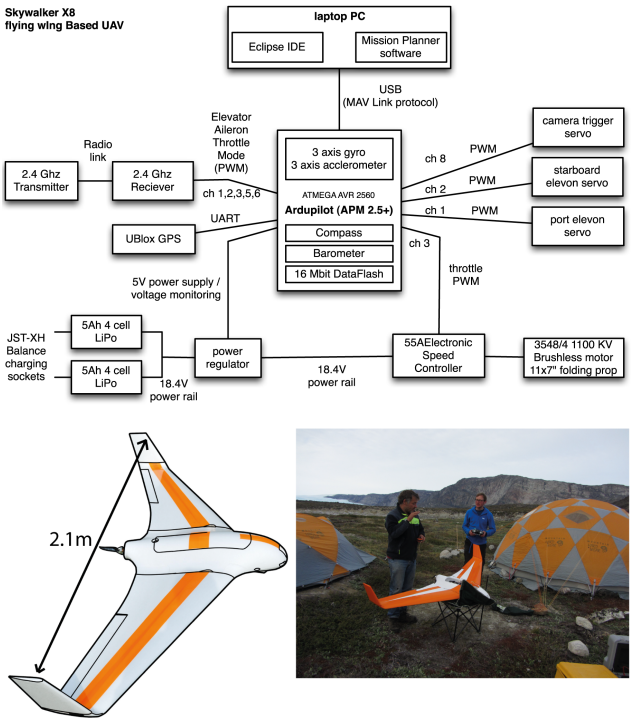

Figure 2. Flowchart of the control set-up and picture of the UAV at base camp with the relative novices.

radio control and pulse-width modulation (PWM) controlled servos for aileron and elevon control (Fig. 2). Ardupilot implements a dual-level proportional-integral-derivative (PID) controller architecture. The lower level controls flight stabilisation and the higher level controls based navigation. Tuning of the PID parameters is necessary to suit the mass and dynamics of the airframe to ensure accurate stabilisation without pitch/roll oscillation (lower-level controller) or flight-path weaving (higher-level controller). The autopilot allows the UAV to fly autonomously according to a pre-programmed flight path defined by a series of 3-D waypoints chosen by the user. The autopilot utilises a GPS for navigation, a triple axis accelerometer and gyro for stabilisation and a barometric pressure sensor for altitude control. These parameters are logged to memory at 10 Hz throughout the flight (Fig. 2).

The advantage of this package is that it can be assembled within a day from off-the-shelf parts and is cost effective at less than USD 2000. The X8 is also relatively straightforward to fly, robust, easily repairable and floats, all added bonuses when being deployed in remote areas by potential novices. Furthermore, the Ardupilot firmware is open source and hence can be programmed for specific requirements, for example camera triggering (see below).

Two lightweight digital cameras were tested at the field site: a Panasonic Lumix DMC-LX5 10.1 megapixel (MP) camera with a 24 mm wide-angle zoom lens and a 16.1 MP Sony NEX-5N with a 16 mm fixed focal length lens though results presented here are limited to the former. A SPOT GPS tracking device was also included in the payload to facilitate recovery should a mission fail (which it did). The focal length of the Lumix lens was adjusted to 5.1 mm (35 mm equivalent) to allow the widest possible coverage which gave the camera a 73.7° horizontal and 53.1° vertical field of view. A short exposure time of 1 / 1600 and a focal ratio of 8 were chosen to prevent overexposure and blurring of the ice surface. The Ardupilot open-source code was amended to trigger the camera automatically at user defined time or distance intervals at or between certain waypoints. The cameras were mounted pointing downwards within the airframe using neoprene and velcro straps to dampen vibration in a custom recessed aperture cut in the bottom with a UV filter to protect the lens and seal it.

2.3 Flight planning

The open-source software APM Mission Planner (http://plane.ardupilot.com/) was used for flight waypoint manipulation and planning in conjunction with the 30 m Greenland Mapping Project (GIMP) DEM (Howat et al., 2014). To optimise spatial coverage against required resolution, flight endurance and stability, the UAV was programmed to fly at a constant altitude of 500 m a.s.l. (Fig. 1). Based on the camera's focal length and field of view (53.1° by 73.7°), the ground (sea-level) footprint at 500 m a.s.l. for each photo was $\sim 450 \times 750$ m. To ensure coverage of the entire glacier terminus and overlap for successful photogrammetric processing, the four transects broadly parallel to the calving front were flown with ~ 250 m separation yielding a side overlap between photos of 70 % (Fig. 1). The mean ground speed of the UAV was $\sim 70\,\mathrm{km\,h^{-1}}$ and the camera trigger interval was adjusted between surveys. On flights 1 and 2, the interval between camera triggers was 1.5 s corresponding to a forward overlap of 94 % and over 1000 geotagged images acquired. Flight 3 had a 2.4 s interval yielding a 90 % forward overlap and 581 images (Table 1).

UAV operations were based out of a field camp with the advantage of a 50 m area of flat alluvial terrace with relatively boulder and bedrock free ground for manual remote-control take-off and landing. This location did, however, require a ~ 10 km transit to the calving front over a 450 m high peninsula which significantly reduced the useful endurance over the target. Of the six sorties flown over outlet glaciers in the region during July and August 2013, the three over Store Glacier were most successful. Each sortie was 40 km long and ~ 35 min in duration after the UAV had attained its operating altitude at the start of the mission and was passed from manual remote-control mode into autopilot mode (Fig. 1). Visual and remote-control contact is lost within a few kilometres of the UAV being placed in autopilot mode; hence, validation of the mission plan is essential.

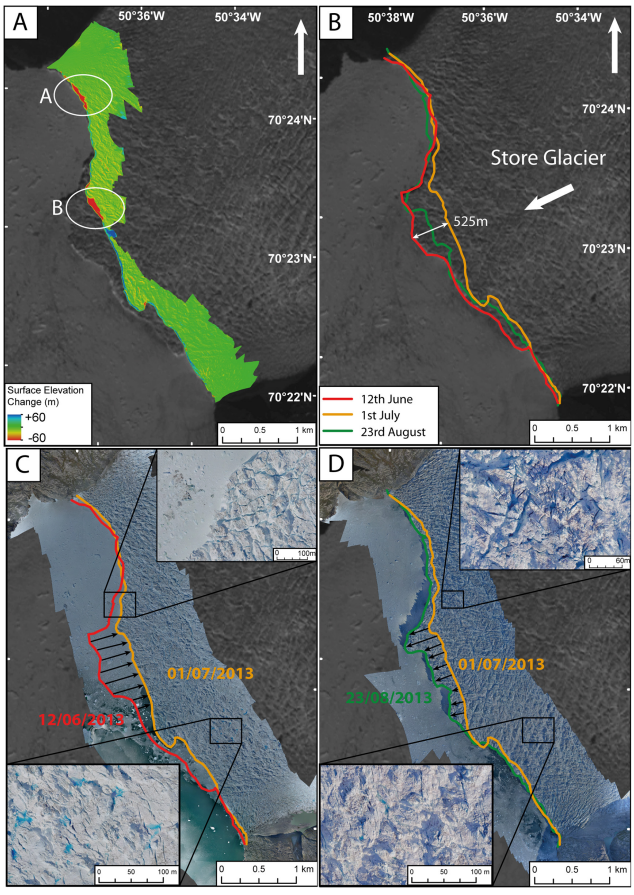

Figure 3. (a) Surface elevation difference between two DEMs collected on 1 July and 2 July. Red areas show elevation loss whilst blue areas show elevation gain. White circles highlight the calving events that occurred between the two UAV surveys. **(b)** The position of the calving front of Store Glacier during the summer of 2013. **(c)** Calving-front retreat observed between 12 June and 1 July. Inset is an orthorectified image of the water-filled crevasses observed on 1 July with a pixel resolution of 30 cm. **(d)** Calving-front advance observed between 1 July and 23 August. Inset is an orthorectified image showing water-filled crevasses observed on 23 August. The coverage and size of water-filled crevasses is smaller.

2.4 Three-dimensional model generation

Three-dimensional data were extracted from the aerial photos using Agisoft PhotoScan Pro software (Agisoft LLC, 2013). This software's strength lies in its ability to fully automate workflow and enables non-specialists to process aerial images and produce 3-D models which can be exported as georeferenced orthophotos and DEMs (e.g. Figs. 3 and 6). The first stage of processing is image alignment using the structure-from-motion (SfM) technique. SfM allows for the reconstruction of 3-D geometry and camera position from a sequence of multiple images and is used to estimate the location of high-contrast features (e.g. edges), obtain the relative location of the acquisition positions and produce a sparse 3-D point cloud of those features. The Ardupilot flight logs of the onboard navigation sensors allow the camera positions and the 3-D point cloud to be georeferenced within instrument precision. SfM also enables the camera calibration parameters (e.g. focal length and distortion coefficients) to be automatically refined; hence, there is no need to pre-calibrate the cameras and lens optics (Verhoeven, 2011).

Once the photos have been aligned, a multi-view reconstruction algorithm is applied to produce a 3-D polygon mesh which operates on pixel values rather than features and enables the fine details of the 3-D geometry to be constructed (Verhoeven, 2011). The user determines the precision of the final 3-D model based on image resolution and pixel footprint. A medium quality setting was chosen yielding DEMs with between 38 and 40 cm/pixel ground sampling resolution (GSD), which were resampled to a Cartesian 50 cm grid to enable intercomparison (Table 1). Higher resolutions (< 30 cm GSD) are attainable but the increase in computational time and the accuracy of georeferencing limits the benefits of such apparent precision.

Two problems of accuracy were encountered in DEM production: (1) PhotoScan failed to reconstruct a flat sea level of constant elevation, and (2) relative positional errors between the DEMs constructed from different sorties were up to 17.12 m horizontally and 11.38 m vertically. Positional errors were due to the specified limits of the onboard L1 GPS of ± 5.0 m horizontally and, when combined with the barometric sensor, to a similar accuracy vertically. These were compounded by the time lag between the camera triggering and actual photograph acquisition. Hence, a secondary stage of processing was carried out which involved 3-D co-registration of the DEMs. To do this, the horizontal and vertical coordinates of common control points (CPs) based on distinct features such as cliff bases, large boulders and promontories were extracted from the georeferenced orthoimages. The CPs that were at sea level were nominally given elevation values of zero, re-imported into PhotoScan and subsequently reprocessed along with a geodetic GPS ground CP located at 70.401° N, −50.665° E and 335.85 m altitude on the bedrock headland overlooking the glacier's northern flank. During this secondary stage of processing, PhotoScan's optimisation procedure was run to correct for possible distortions. After processing with the CPs, a flat sea level across the glacier front was produced and the relative errors between the three DEMs were reduced to ± 1.41 m horizontally and ± 1.90 m vertically. The georeferenced 3-D DEMs and orthophotos were then exported at 50 cm pixel size for further analysis in ArcGIS and ENVI software packages.

2.5 Analysis

Changes in calving-front positions were obtained from these data combined with a Landsat 8 panchromatic image obtained on 12 June (Fig. 3b). Each calving-front position was digitised according to the procedure outlined by Moon and Joughin (2008), whereby a polygon of the calving-front retreat or advance is digitised and divided by the width of the glacier. This method has been used in previous studies (e.g. Howat et al., 2010; Schild and Hamilton, 2013) and enables intercomparison of results. Surface elevation change was calculated from the residual difference of the DEMs (Fig. 3a).

Ice flow across the terminus region was calculated by feature tracking performed on successive DEMs using the ENVI Cosi-CORR software module (Fig. 4b). These velocities were then used to estimate ice flux through the calving front for the same period under the assumption of plug flow (uniform velocity profile with depth) and using a calving-front cross section obtained from Xu et al. (2013) and modified by single and multi-beam echo sounder bathymetry obtained by S/V *Gambo* in 2010 and 2012 (Chauché, unpublished). The frontal cross section was divided into 10 m vertical strips and under the plug-flow assumption, each was assigned its corresponding horizontal velocity (Fig. 4a). The floatation depth and buoyancy ratio across the calving front was calculated using the ice surface (freeboard) elevation and total ice thickness with a value for the density of ice of 917 $\mathrm{kg\,m^{-3}}$ and for sea water of 1028 $\mathrm{kg\,m^{-3}}$ (Fig. 5a).

To investigate the distribution and patterns of crevassing, each DEM was Gaussian filtered at 200 pixels (100 m) in ArcGIS and subtracted from the original DEM to yield the pattern of negative surface anomalies. These anomalies were converted into polygons to map and hence quantify crevasse distribution and character (Fig. 6a). The resulting polygons were enclosed by a minimum bounding rectangle, which allowed the orientation, width, length and depth of crevasses to be extracted (Fig. 6a, Table 2). Water-filled crevasses were automatically located in the ENVI package using the supervised maximum likelihood classification (MLC) method. Representative training samples for water-filled areas were chosen from the colour composite orthophoto (Fig. 6b). The trained tool then classifies pixels that are interpreted as water into the desired class. The resulting raster image was converted into a shapefile and used to mask and define the area of the water-filled crevasses across the terminus. These procedures allow thousands of crevasses in multiple orthoimages and DEMs to be quantified easily without the difficulties and dangers associated with direct field measurements.

2.6 Uncertainties and limitations

The relative horizontal uncertainties between the DEMs were investigated by feature tracking the stationary bedrock at the sides of the glacier. The root mean square (rms) horizontal displacement was ± 1.41 m which provides us with an approximate error estimate. The relative vertical uncertainties between the DEMs were estimated by calculating elevation differences between bedrock areas, which revealed an error estimate of ± 1.9 m. The two-stage procedure outlined in Sect. 2.4 therefore enabled us to improve the relative positional uncertainties from nearly 20 m to less than 2 m. For future studies, it is thought that several CPs on the bedrock either side of the glacier front would further reduce these uncertainties. A telemetric differential GPS deployed on or near the calving front, which is sufficiently large/bright to identify within the aerial imagery would allow further ground control in the centre of DEMs, away from bedrock CPs.

Due to the lack of reflected light from deep crevasse recesses, the DEM generation process cannot quantify the narrowest sections of all fractures and resultant crevasse depths are therefore a minimum estimate. The technique is also clearly limited to line of sight precluding narrow fractures which extend for tens of centimetres horizontally and potentially up to a few metres vertically (Hambrey and Lawson, 2000; Mottram and Benn, 2009).

Finally, there are a number of practical difficulties when operating an autonomous aircraft in remote and inaccessible environments. Mission planning is critical; knowledge of the local weather conditions, as well as up-to-date satellite imagery and DEMs are a prerequisite.

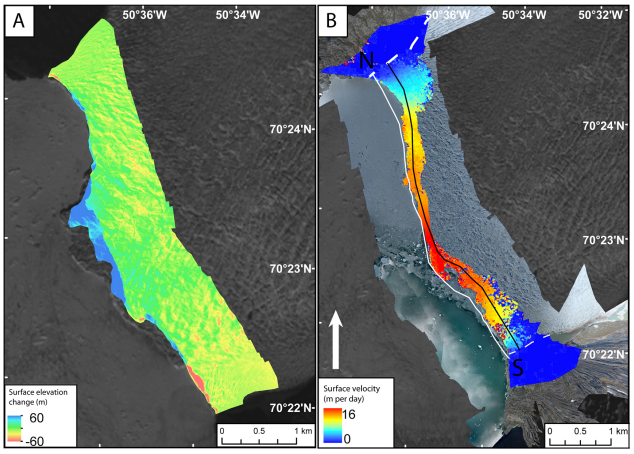

Figure 4. (a) Surface elevation changes between 2 July and 23 August. An average thinning of 0.12 $\mathrm{m\,d^{-1}}$ was estimated for the surveyed area. **(b)** The ice-flow speed structure of the terminus of Store Glacier between 1 and 2 July 2013. The centre of the glacier flows at approximately 16 $\mathrm{m\,d^{-1}}$ whilst the margins flow less than 5 $\mathrm{m\,d^{-1}}$. Dotted white lines show the lateral margins of the glacier. The black line represents the locations of the horizontal velocity and surface elevation values that were used to estimate ice flux. The white line represents the location of the depth values used to estimate ice flux. The cross section of the calving front derived from these profiles is displayed in **(a)**.

Table 2. Attributes of mean crevasse width, length and orientation in each zone labelled in Fig. 5. Orientations are measured along the long axis of each crevasse with respect to the direction of flow which is 0°.

Zone	Mean width (m)	Mean length (m)	Mean orientation (°)
Zone 1	3.6	9.4	9.2
Zone 2	4.8	14.0	36.7
Zone 3	10.5	32.6	85.1
Zone 4	6.5	17.8	60.4
Zone 5	3.5	8.5	10.8

3 Results

Three successful UAV sorties were flown over Store Glacier calving front providing imagery, orthophotos and DEMs on 1 and 2 July and the 23 August, herein referred to as flights and associated products 1 to 3, respectively (Table 1). The interval between flights 1 and 2 was 19 hours and comparison between these outputs enables identification of processes operating over a daily (short) timescale, be it a very specific snapshot. The third sortie was flown 52 days later and comparison between these outputs enables investigation of late-seasonal change. The footprint of the four cross-glacier transects flown extends just over 1 km upstream from the calving front and herein is referred to as the terminus.

3.1 Short timescale calving and surface elevation change

Residual elevation change between 1 and 2 July (Fig. 3a) reveals that the front retreated in two sections by up to 50 and 80 m, respectively. The more northerly calving event (A) resulted in a 450 m wide section of the terminus retreating by between 20 and 50 m, whilst event B produced between 20 and 80 m of retreat across a 400 m section (Fig. 3a). In addition to these two calving events (which are discussed in section 3.6), the central 4.5 km frontal section advanced between 12 to 16 m (Fig. 3a). At its lateral margins, the calving front shows no discernible systematic change though there are isolated, small calving events, for example, within 50 m of the southern flank (Fig. 3a). Upstream of the calving front, there is no net change in mean surface elevation away from the front and the dappled pattern of residual elevation change is a result of the advection of crevasses and seracs. Successive long profiles of the terminus between the 1 and 2 July reveal specific down-glacier crevasse advection with flow (Fig. 6) at a rate of 5 and 16 m d^{-1} on profile 1 and 2, respectively. These results provide corroboration for the surface velocities derived by feature tracking in Sect. 3.4.

3.2 Seasonal timescale calving-front position and surface elevation change

Over the entire melt season, larger fluctuations in calving-front position are observed (Fig. 3b). Over the 19-day period from 12 June to 1 July, mean frontal retreat was 160 m (Fig. 3c) and between 2 July and 23 August, the calving front advanced by an average of $\sim$ 110 m to a position similar to that in 12 June (Fig. 3d). These mean values, however, do not convey the full extent and detail of the changes observed in the calving front. For example, the central section of the calving front retreated by up to 525 m between the 12 June and 1 July and advanced by up to 450 m between 2 July and 23 August (Fig. 3b). Furthermore, the lateral margins of Store Glacier (the southern 850 m and the northern 1.5 km) are relatively stable with < 50 m change in position. Over the 52-day period between 2 July (Flight 2) and 23 August (Flight 3) widespread surface lowering of 6.1 m (or 0.12 m d^{-1}) was observed across Store Glacier terminus (Fig. 4a), which is significantly larger than the estimated vertical uncertainties of the DEMs ($\pm$ 1.9 m). Despite the same dappled patterns caused by local advection of crevasses and seracs, we infer this to be associated with dynamic thinning 1 km upstream of the calving front, which is discussed in Sect. 4.2.

3.3 Bathymetry

The deepest sector of the calving front is located 1 km south of the centreline and exceeds 540 m below sea level (Fig. 5a). This 200 m wide sector also corresponds to the greatest thickness of $\sim$ 600 m. To the south of this deepest point, the bottom rises rapidly to a 200 m deep shelf located 500 m from the flank. To the north of the deepest point, the bottom shallows more gently to within 400 m where it becomes steeper towards the fjord wall.

3.4 Surface velocities

Maximum surface-flow velocities of 16 m d^{-1} between 1 and 2 July are consistent with results obtained in previous studies using other techniques, such as feature tracking images from a land-based time-lapse camera (between 11 and 15 m d^{-1}) (Ahn and Box, 2010; Walter et al., 2012). The spatial pattern of surface flow from feature tracking of images between the 1 and 2 July varies considerably across the terminus of Store Glacier (Fig. 4b) attaining velocities of 16 m d^{-1} (5.8 km a^{-1}) near the centre of the glacier down to 2.5 m d^{-1} at the lateral flanks. Surface velocities are related to slope, depth, thickness and distance from the lateral margins (Fig. 5c, d). As would be expected, maximum velocities correlate with maximum depth and towards the northern flank are linearly correlated ($R^2 = 0.90$) with frontal depth (Fig. 5c). Towards the southern flank the relationship is less apparent especially between 200 and 350 m depths. There

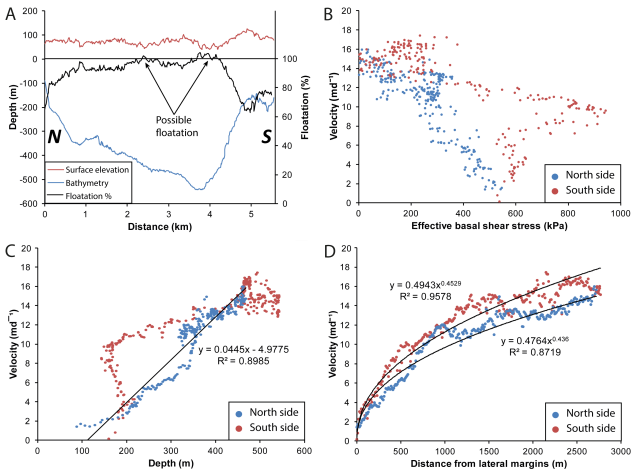

Figure 5. (a) Profiles showing the sea floor bathymetry and ice surface elevation at the calving front. These data were combined with surface velocities to estimate the ice flux of Store Glacier. Where the floatation percentage is over 100 %, it is assumed that the ice is not thick enough to be fully grounded in hydrostatic equilibrium. **(b)** The relationship between effective basal shear stress and velocity. **(c)** The relationship between depth and velocity. At depths deeper than 400 m, velocities are fairly constant. The two differing relationships between 150 and 350 m represent velocities from different sides of the glacier. **(d)** Relationship between velocity and distance from the lateral margins. The positive correlation demonstrates the importance of the resistance provided by the fjord walls.

is a strong correlation between velocities and distance from the lateral margins which can be approximated by a power function ($R^2 = 0.90$) (Fig. 5d). Although application of the floatation criteria reveals parts of calving front to be buoyant (Fig. 5a), side-scan sonar observations reveal that the glacier toe was resting on the fjord bed (Chauché, unpublished). When the surface flow pattern is combined with frontal bathymetric data we estimated that the mass flux through the calving front of Store Glacier was $3.8 \times 10^7\,\mathrm{m^3\,d^{-1}}$, equivalent to $\sim 13.9\,\mathrm{Gt\,a^{-1}}$.

Seasonal flow patterns were not obtainable between 2 July and 23 August as the majority of any matching features within the study area required for tracking had already calved into the ocean. Furthermore, it is likely that the morphology of many crevasses and seracs will have changed significantly through melt and deformation and would not be recognised by the cross-correlation procedure.

3.5 Crevassing

The morphology and orientation of crevasses varies markedly across the terminus (Fig. 6). The largest crevasses occur in a sector south of the glacier centre line in zone 4 (Fig. 6, Table 2). Here, crevasses have mean minimum depths of 18 m, lengths of 68 m and widths of 31 m. The largest crevasses are up to 30 m deep, over 500 m long and nearly 200 m wide but no crevasses that penetrated below sea level were identified. Most crevasses in this region are arcuate with limbs pointing towards the calving front and are orientated obliquely to the direction of ice flow (Fig. 6). This arcuate morphology of crevasses continues across the central 3 km of the terminus in zone 3 (Fig. 6). Here, crevasses have mean a depth of 10.5 m, length of 50 m and widths of 18 m (Table 2). In zone 2, 300 to 500 m from the northern flank, crevasses are aligned obliquely to the direction of ice flow (30–45°). Up to the fjord walls in zones 1 and 5, crevasses are generally orientated parallel to the ice flow (> 15°) (Fig. 6, Table 2) and are much smaller with a mean lengths of 22 m and width of 8 m (Table 2). No discernible difference in average crevasse depths, lengths or widths was observed between early July and late August and the pattern and character of crevassing was also similar.

Water-filled crevasses were clustered in zone 4, coinciding with the sector of larger crevasses (Fig. 6b). Water-filled crevasses covered 12 000 $\mathrm{m^2}$ or 0.24 % of the survey area (to ~ 1 km from the calving front) on 2 July (Table 1). Some 42 individual water-filled crevasses were identified with the largest having an area of 1200 $\mathrm{m^2}$. By 23 August, the number, size and total area of water-filled crevasses were lower: only 10 water-filled crevasses could be identified, the largest of which was 400 $\mathrm{m^2}$ and with a total area of 1230 $\mathrm{m^2}$ (0.025 % of the survey area). We were not able to ascertain the depth of water in the crevasses as no common crevasses could be identified which drained or filled between flights but this would be a specific aim of future studies which, with regular sorties, could potentially determine the depth of a crevasse before filling or after drainage or otherwise exploit the light reflectance relationship with water depth (e.g. Fitzpatrick et al., 2014).

Successive profiles of the terminus from 1 and 2 July demonstrate how the UAV surveys are capable of capturing the displacement of crevasses, which advect downstream at a rate of 5 and 16 $\mathrm{m\,d^{-1}}$ in profiles 1 and 2, respectively (Fig. 6). The techniques used in this study are therefore capable of identifying changes in crevasses geometry, particularly width and depth through time.

3.6 Calving events

The two calving events identified between 1 and 2 July appear to take place under contrasting conditions. Event A consisted of the calving of multiple, relatively small ice blocks with the glacier failing along two main crevasses located 30 and 50 m behind the calving front. These crevasses were between 8 and 10 m deep, respectively, and in this instance, the crevasses located closest to the front were the ones that failed. Event B appears to be a single large event caused by the fracturing of a series of parallel crevasses which were up to 14 m deep and 60 m behind the calving front. Unlike, calving event A, the crevasses that failed in event B were not the closest to the calving front. Indeed, there were other

crevasses that were deeper and located nearer to the front, yet did not calve. Water was not observed in any of the crevasses along which calving took place.

4 Discussion

4.1 Changes occurring over a daily timescale

The orientation of crevasses suggests that lateral drag is an important resistive stress on Store Glacier. The lateral margins of Store Glacier are characterised by crevasses that are orientated parallel to the direction of flow which suggests that they have formed in response to simple shear stresses associated with the drag of the fjord walls (Fig. 6) (Benn and Evans, 2010). The importance of lateral drag is further demonstrated by the morphology of crevasses found near the glacier flow line (Fig. 6). Their arcuate nature indicates that the principal tensile stresses operating on the ice have been rotated by lateral gradients in ice velocity. These gradients are caused by the simple shear stress between the fjord walls and the margins of the glacier which cause the ice to flow slower (Fig. 4b) (Benn and Evans, 2010).

The simple shearing caused by velocity gradients is further demonstrated by the differing relationship between velocity and depths between the north and south side of the glacier (Fig. 5c, d). On the north side, the velocity increases gradually from the fjord wall to the centre of the glacier, reflecting the gradual deepening of bathymetry and the resulting decrease of basal and lateral drag. On the south side, the velocities are higher than the north side for given depths and distances from the lateral margins (Fig. 5c, d). We hypothesise that, because the deepest part of the glacier is situated 1 km south of the centreline, the ice on south side is more influenced by faster flowing ice which exerts a simple shear stress on the shallower, adjacent ice (250–400 m thick). This causes the shallow ice to flow faster than ice with similar thicknesses and distance from the lateral margins on the north side (Fig. 5c).

The mass flux through the calving front was calculated at $3.8 \times 10^7\ m^3\ d^{-1}$ which needs to be balanced by three main frontal processes: calving, submarine melting and advective advance. Both calving and advance were observed in this study but it is likely that submarine melting also has a large role in ice output at a daily timescale. For example, Xu et al. (2013) used oceanographic data to calculate a melt water flux of between 0.5 and $1.1 \times 10^7\ m^3\ d^{-1}$ from Store Glacier in August 2010 equivalent to 13–29 % of the mass flux calculated by our study. For comparison, Rink glacier has an ice flux of $3.0 \times 10^7\ m^3\ d^{-1}$ of which 27 % is estimated to be lost through submarine melting each day (Enderlin and Howat, 2013).

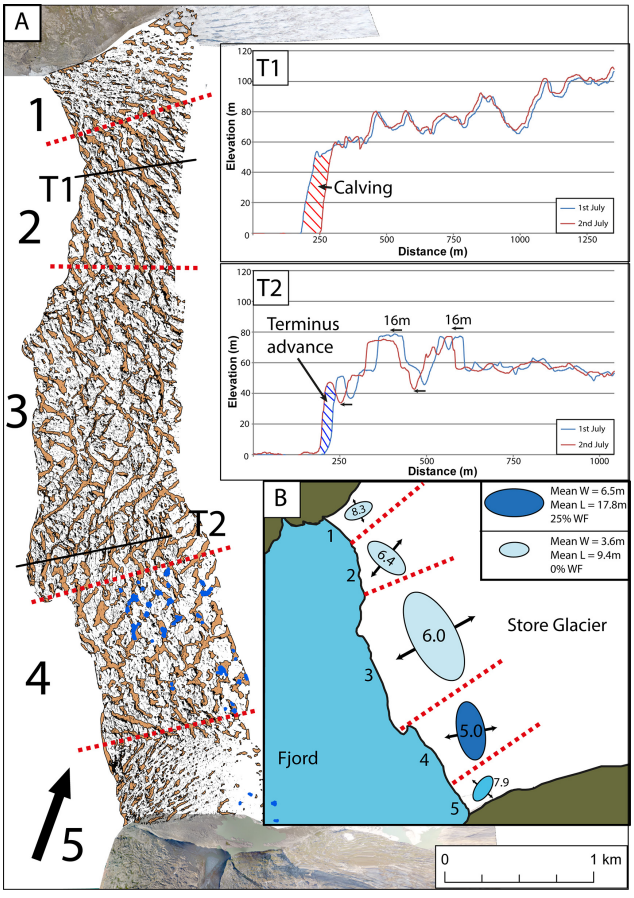

Figure 6. (a) Distribution and patterns of crevasses on Store Glacier. Dry crevasses, which are large structural features, are shown in orange. Narrower crevasses that are observed in the orthorectified images but whose 3-D geometry is not constructed are shown in black. The areas of water-filled crevasses are shown in blue and occur almost exclusively in zone 4. The regions of the terminus discussed are designated by the dotted red lines and are referred to as the black numbers. Transects 1 and 2 shown in the inset demonstrate how crevasses adverted downstream between 1 and 2 July. In T1, a series of calving events occurred which are discussed as calving event A. In T2, the calving front advanced 16 m. **(b)** Illustration of the terminus of Store Glacier with ellipsoids proportional to the average length, width and orientation of crevasses shown in **(a)** for the respective zones. The colour of the ellipsoids represents the proportion of crevasses that are water filled in each zone where WF refers to water filled in the legend. The italicised numbers denote the density of crevasses per $10\ m^2$ in each zone. Arrows illustrate inferred direction of principal strain.

4.2 Changes occurring over a seasonal timescale

The lack of variation in the position of the lateral margins of the glacier shows that a balance is maintained between the ice flux input and submarine melting and calving output in this zone throughout the melt season. The balance could be explained by the mechanism of calving events. At the lateral margins calving is characterised by small, regu-

lar events such as calving event A (Fig. 3a). The regularity of these small events means that any small advance or retreat is regulated almost instantly by changes in calving rate which returns the lateral margins of the glacier to the same position. Calving rate could also be moderated by changes in the bathymetry. When the lateral margins advance, calving rates increase due to the abrupt deepening of the bathymetry seaward of the lateral margins of the glacier which cause basal drag to be reduced. Ice-flow acceleration can lead to increased longitudinal stretching and deeper crevassing, thereby increasing calving rate and leading to retreat to its original, bathymetrically pinned position.

The centre of the calving front is much more active with calving and submarine melt rates that vary on a seasonal timescale. We propose that the main cause of variability is due to calving rates which are highly irregular throughout the melt season (Jung et al., 2010). Our observations also support the suggestion that calving rates are dominated by major calving events which have a time interval of around 28 days (e.g. Jung et al., 2010). If the calving front advances for 28 days at $16\,\mathrm{m\,d^{-1}}$, it will advance $\sim 448\,\mathrm{m}$. A large, single calving event can therefore yield a retreat of $\sim 448\,\mathrm{m}$ and would explain the variation in the position of the calving front during the melt season (Fig. 3b). On 25 August 2013, a tabular iceberg with a length of $\sim 500\,\mathrm{m}$ was observed to calve from the central zone of Store Glacier.

Towards the end of the melt season (23 August), a widespread surface deflation of $0.12\,\mathrm{m\,d^{-1}}$ was observed (Fig. 4a). Application of a simple degree-day model reveals that part of this lowering can be attributed to ablation. Average daily air temperatures were recorded at an automated weather station (AWS) located near the UAV launch site (Fig. 1) and, using a melt factor of 6–10 mm per degree per day (Hock et al., 2005), surface lowering due to ablation is estimated between 0.038 and $0.064\,\mathrm{m\,d^{-1}}$. It follows that ablation alone cannot account for the entire lowering rate observed and, hence, we infer an additional component of dynamic thinning due to relative strain extension across this zone, related to reduced upstream delivery of flux and/or frontal kinematics associated with enhanced late-season submarine melting and/or calving rates. GPS measurements by Ahlstrom et al. (2013) tentatively support the former interpretation and reveal that surface velocities 8 km upstream of Store's calving front tend to decrease between July and August. However, this raises questions regarding the timescales over which dynamic thinning and surface melt occur and whether or not the flow regime across the terminus is, to some extent, isolated or operating independent from processes upstream supplying mass. Either way, these questions are beyond the scope of the data sets presented here and require a study of greater areal extent and temporal coverage.

Another important observation is the order of magnitude reduction of the area of water-filled crevasses between early July and late August (Fig. 6). Surface air temperatures directly influence the extent of water-filled crevasses. AWS data reveal that mean daily air temperature was $\sim 6\,^{\circ}\mathrm{C}$ during the 4 days prior to the UAV sortie on the 2 July. In contrast, mean temperature was $\sim 3.5\,^{\circ}\mathrm{C}$ on the 4 days prior to the UAV sortie on 23 August. Water-filled crevasses have been hypothesised to penetrate deeper than crevasses without water (Weertman, 1973; van der Veen, 1998) and hence act as mechanism for calving (Benn et al., 2007). The calving events observed in this study did not specifically fail at water-filled crevasses and hence our limited results show no support for this mechanism. However, studies of greater scope with daily coverage will be required to determine definitively if water-filled crevasses have any appreciable impact on calving dynamics at Store Glacier or elsewhere.

5 Conclusions and future directions

A UAV equipped with a commercial digital camera enabled us to obtain high-resolution DEMs and orthophotos of the calving front of a major tidewater glacier at an affordable price. Airborne lidar currently presents the only alternative method for acquiring DEMs with comparable accuracy and precision. However, to fly consecutive sorties in a remote environment is likely to be prohibitively expensive and with sufficient ground control points the digital photogrammetry approach may also exceed the accuracy of this technique.

The three sorties flown enabled key glaciological parameters to be quantified at sufficient detail to reveal that the terminus of Store Glacier is a complex system with large variations in crevasse patterns surface velocities, calving processes, surface elevations and front positions at a daily and seasonal timescale. Surface velocities vary across the terminus and are influenced by both basal and lateral drag (Figs. 4b and 5c, d). The oblique orientation and arcuate nature of crevasses suggests that the principal extending strain rate is orientated obliquely to the direction of flow and we therefore propose that resistive stresses at the terminus of Store Glacier are dominated by lateral drag (Fig. 6). With this in mind, the retreat of Store Glacier into a wider trough could significantly increase the ice discharge. We estimated that the ice flux through the calving front of Store Glacier was $13.9\,\mathrm{Gt\,a^{-1}}$ and we observed a small terminus advance between 1 and 2 July (Figs. 3a and 5a). This advance reveals that, during this period, the sum of calving and submarine melt rates are less than the ice flux. Calving is an irregular process and that the position of the calving front returned to its 12 June position by 23 August suggests that over this timescale calving and submarine melting balance ice flux (Fig. 3b). Water-filled crevasses covered 0.24 % of the survey area on 2 July but this fell to 0.025 % on 23 August (Fig. 6). It remains to be seen whether water-filled crevasses are more likely to initiate calving events but our tentative results here indicate no support for this mechanism.

Future studies, with more frequent sorties could be used to compare and investigate further glaciological changes over

a more continuous timespan. There is also the possibility of more sophisticated payloads with radiation, albedo and other multi-band sensors as well as radar and laser altimetry. There are many potential cryospheric applications for investigation, such as sea ice, marine and terrestrial-terminating glaciers and, with increased range, ice sheets, that can be achieved with the use of repeat UAV surveys. We have demonstrated that for calving outlet glaciers, a UAV carrying a high-resolution digital camera would be sufficient to investigate the following projects:

- analysis of the thickness and back stress exerted by the ice mélange during the winter and the effect of its break out on glacier flow, calving rate and character;
- seasonal changes in the depth, density, orientation and nature of crevassing and their impact on calving rate and character;
- the influence of daily to seasonal melt and supraglacial lake drainage on downstream dynamics and calving;
- analysis of daily to seasonal fluctuations in calving flux, terminus position and impact on upstream dynamics and thinning.

Acknowledgements. We thank Matt Nolan, Doug Benn and Mauri Pelto for their thorough and insightful reviews, and Anders Damsgaard for his short comments: all of which greatly improved the manuscript. Funding for the fieldwork was made possible by the UK Natural Environmental Research Council (NERC) grant NE/K005871/1 (Subglacial Access and Fast Ice Research Experiment (SAFIRE): Resolving the Basal Control on Ice Flow and Calving in Greenland). NERC also funded *The Cryosphere* page charges. J. C. Ryan is funded by an Aberystwyth University Doctoral Career Development Scholarship (DCDS). We are also indebted to the crew of S/V *Gambo* who worked tirelessly to provide logistical support, and to the Uummannaq Polar Institute and Children's Home who provided accommodation in Uummannaq.

Edited by: A. Kääb

References

AgiSoft LLC: AgiSoft PhotoScan, available at: http://www.agisoft.ru/products/photoscan/ (last access: 14 February 2014), 2013.

Ahlstrøm, A. P., Andersen, S. B., Andersen, M. L., Machguth, H., Nick, F. M., Joughin, I., Reijmer, C. H., van de Wal, R. S. W., Merryman Boncori, J. P., Box, J. E., Citterio, M., van As, D., Fausto, R. S., and Hubbard, A.: Seasonal velocities of eight major marine-terminating outlet glaciers of the Greenland ice sheet from continuous in situ GPS instruments, Earth Syst. Sci. Data, 5, 277-287, doi:10.5194/essd-5-277-2013, 2013.

Ahn, Y. and Box, J. E.: Glacier velocities from time-lapse photos: technique development and first results from the Extreme Ice Survey (EIS) in Greenland, J. Glaciol., 56, 723–734, doi:10.3189/002214310793146313, 2010.

Benn, D. I., Warren, C. R., and Mottram, R. H.: Calving processes and the dynamics of calving glaciers, Earth-Sci. Rev., 82, 143–179, doi:10.1016/j.earscirev.2007.02.002, 2007.

Benn, D. I. and Evans, D. J. A.: Glaciers and glaciation, London: Hodder Education, 2010.

Carr, J. R., Vieli, A., and Stokes, C. R.: Climatic, oceanic and topographic controls on marine-terminating outlet glacier behavior in north-west Greenland at seasonal to interannual timescales, J. Geophys. Res., 118, 1210–1226, 2013.

d'Oleire-Oltmanns, S., Marzolff, I., Peter, K. D., and Ries, J. B.: Unmanned Aerial Vehicle (UAV) for monitoring soil erosion in Morocco, Remote Sens., 4, 3390–3416, 2012.

Enderlin, E. M. and Howat, I. M.: Submarine melt rate estimates for floating termini of Greenland outlet glaciers (2000–2010), J. Glaciol., 59, 67–75, doi:10.3189/2013jog12j049, 2013.

Fitzpatrick, A. A. W., Hubbard, A. L., Box, J. E., Quincey, D. J., van As, D., Mikkelsen, A. P. B., Doyle, S. H., Dow, C. F., Hasholt, B., and Jones, G. A.: A decade (2002–2012) of supraglacial lake volume estimates across Russell Glacier, West Greenland, The Cryosphere, 8, 107–121, doi:10.5194/tc-8-107-2014, 2014.

Hambrey, M. J. and Lawson, W.: Structural styles and deformation fields in glaciers: A review, Deform. Glacial Mater., 176, 59–83, doi:10.1144/Gsl.Sp.2000.176.01.06, 2000.

Hock, R.: Glacier melt: a review on processes and their modelling, Progr. Phys. Geogr., 29, 362–391, 2005.

Holland, D. M., Thomas, R. H., De Young, B., Ribergaard, M. H., and Lyberth, B.: Acceleration of Jakobshavn Isbrae triggered by warm subsurface ocean waters, Nat. Geosci., 1, 659–664, doi:10.1038/Ngeo316, 2008.

Howat, I. M., Joughin, I., and Scambos, T. A.: Rapid changes in ice discharge from Greenland outlet glaciers, Science, 315, 1559–1561, doi:10.1126/science.1138478, 2007.

Howat, I. M., Box, J. E., Ahn, Y., Herrington, A., and McFadden, E. M.: Seasonal variability in the dynamics of marine-terminating outlet glaciers in Greenland, J. Glaciol., 56, 601–613, 2010.

Howat, I. M., Negrete, A., and Smith, B. E.: The Greenland Ice Mapping Project (GIMP) land classification and surface elevation data sets, The Cryosphere, 8, 1509–1518, doi:10.5194/tc-8-1509-2014, 2014.

Hubbard, A.: The Times Atlas and actual Greenland ice loss, Geol. Today, 27, 214–217, 2011.

Hugenholtz, C. H., Levin, N., Barchyn, T. E., and Baddock, M. C.: Remote sensing and spatial analysis of aeolian sand dunes: A review and outlook, Earth-Sci. Rev., 111, 319–334, doi:10.1016/j.earscirev.2011.11.006, 2012.

Hugenholtz, C. H., Whitehead, K., Brown, O. W., Barchyn, T. E., Moorman, B. J., LeClair, A., Riddell, K., and Hamilton, T.: Geomorphological mapping with a small unmanned aircraft system (sUAS): Feature detection and accuracy assessment of a photogrammetrically-derived digital terrain model, Geomorphology, 194, 16–24, doi:10.1016/j.geomorph.2013.03.023, 2013.

Joughin, I., Das, S. B., King, M. A., Smith, B. E., Howat, I. M., and Moon, T.: Seasonal speedup along the western flank of the Greenland ice sheet, Science, 320, 781–783, doi:10.1126/science.1153288, 2008.

Joughin, I., Smith, B. E., Howat, I. M., Floricioiu, D., Alley, R. B., Truffer, M., and Fahnestock, M.: Seasonal to decadal scale variations in the surface velocity of Jakobshavn Isbrae, Greenland:

Observation and model-based analysis, J. Geophys. Res.-Earth Surf., 117, F02030, doi:10.1029/2011jf002110, 2012.

Jung, J., Box, J. E., Balog, J. D., Ahn, Y., Decker, D. T., and Hawbecker, P.: Greenland glacier calving rates from Extreme Ice Survey (EIS) time lapse photogrammetry, C23B-0628, American Geophysical Union, San Francisco, 2010.

Kargel, J. S., Ahlstrøm, A. P., Alley, R. B., Bamber, J. L., Benham, T. J., Box, J. E., Chen, C., Christoffersen, P., Citterio, M., Cogley, J. G., Jiskoot, H., Leonard, G. J., Morin, P., Scambos, T., Sheldon, T., and Willis, I.: Brief communication Greenland's shrinking ice cover: "fast times" but not that fast, The Cryosphere, 6, 533–537, doi:10.5194/tc-6-533-2012, 2012.

Lucieer, A., Turner, D., King, D. H., and Robinson, S. A.: Using an Unmanned Aerial Vehicle (UAV) to capture micro-topography of Antarctic moss beds, Int. J. Appl. Earth Observ.Geoinform., 27, 53–62, 2014.

Luckman, A., Murray, T., de Lange, R., and Hanna, E.: Rapid and synchronous ice-dynamic changes in East Greenland, Geophys. Res. Lett., 33, L03503, doi:10.1029/2005GL025428, 2006.

Moon, T. and Joughin, I.: Changes in ice front position on Greenland's outlet glaciers from 1992 to 2007, J. Geophys. Res.-Earth Surf., 113, F02022, doi:10.1029/2007jf000927, 2008.

Mottram, R. H. and Benn, D. I.: Testing crevasse-depth models: A field study at Breioamerkurjokull, Iceland, J. Glaciol., 55, 746–752, doi:10.3189/002214309789470905, 2009.

Schild, K. M. and Hamilton, G. S.: Seasonal variations of outlet glacier terminus position in Greenland, J. Glaciol., 59, 759–770, doi:10.3189/2013jog12j238, 2013.

Ullman, S.: The interpretation of structure from motion, Proc. Roy. Soc. London, B203, 405–426, 1979.

van der Veen, C.: Fracture mechanics approach to penetration of bottom crevasses on glaciers, Cold Reg. Sci. Technol., 27, 213–223, 1998.

Verhoeven, G.: Taking computer vision aloft – archaeological three-dimensional reconstructions from aerial photographs with Photoscan, Archaeol. Prospection, 18, 67–73, 2011.

Vieli, A., Funk, M., and Blatter, H.: Tidewater glaciers: Frontal flow acceleration and basal sliding, Ann. Glaciol., 31, 217–221, doi:10.3189/172756400781820417, 2000.

Xu, Y., Rignot, E., Fenty, I., Menemenlis, D., and Flexas, M. M.: Subaqueous melting of Store Glacier, West Greenland from three-dimensional, high-resolution numerical modeling and ocean observations, Geophys. Res. Lett., 40, 4648–4653, doi:10.1002/Grl.50825, 2013.

Walter, J. I., Box, J. E., Tulaczyk, S., Brodsky, E. E., Howat, I. M., Ahn, Y., and Brown, A.: Oceanic mechanical forcing of a marine-terminating Greenland glacier, Ann. Glaciol., 53, 181–192, doi:10.3189/2012aog60a083, 2012.

Weertman, J.: Can a water-filled crevasse reach the bottom surface of a glacier?, IAHS Publ., 95, 139–145, 1973.

Whitehead, K., Moorman, B. J., and Hugenholtz, C. H.: Brief Communication: Low-cost, on-demand aerial photogrammetry for glaciological measurement, The Cryosphere, 7, 1879–1884, doi:10.5194/tc-7-1879-2013, 2013.

Weidick, A.: Greenland, with a section on Landsat images of Greenland, in, Satellite image atlas of glaciers of the world, edited by: Williams, R. S. and Ferrigno, J. G., US Geological Survey, Washington, DC, C1–C105 (USGS Professional Paper 1386-C), 1995.